



Cite this: *Energy Environ. Sci.*, 2024, 17, 5691

Engineering a molecular electrocatalytic system for energy-efficient ammonia production from wastewater nitrate†

Dean M. Miller, ^a Matthew J. Liu, ^a Kristen Abels, ^a Anna Kogler, ^b Kindle S. Williams ^a and William A. Tarpeh ^{*abc}

Anthropogenic ammonia production has sustained exponential population growth but exacerbated wastewater nitrate pollution. Abundant nitrate can be refined to purified nitrogenous chemicals through the electrochemical nitrate reduction reaction (NO_3RR). However, the dilute and impure composition of nitrate-bearing wastewaters presents barriers to practical electrocatalytic systems. We address these barriers in our investigation of the model ammonia-selective homogeneous molecular NO_3RR catalyst $\text{Co}(\text{DIM})$ in real wastewater and reactive separations architectures. In this work, we elucidate catalysis inhibition mechanisms imposed by magnesium in real wastewaters that decrease nitrate conversion activity by 62.0%. These mechanisms informed our design of electrocatalyst-in-a-box (ECaB), a novel NO_3RR reactive separation that exhibits the lowest reported energy consumption for purified wastewater-derived ammonia production ($90.0 \pm 2.7 \text{ kW h kg N}^{-1}$). Engineering ECaB's subunit processes enhanced the rate of ammonia production by 20.4×. This work demonstrates a use-informed engineering approach that iterates between mechanistic insights and unit process-level performance of electrochemical wastewater refining systems in complex aqueous streams.

Received 19th April 2024,
Accepted 21st June 2024

DOI: 10.1039/d4ee01727g

rsc.li/ees

Broader context

Wastewater refining generates valuable products from aqueous waste streams. While promising for chemical manufacturing, wastewaters are dilute and impure. These challenges have generally precluded the use of molecular catalysts for wastewater treatment. We evaluated the potential for a cobalt-centered molecular catalyst to convert wastewater nitrate into high-purity ammonia by systematically identifying wastewater constituents that interfered with catalytic activity. With these insights, we designed a novel electrochemical reactive separation process, electrocatalyst-in-a-box (ECaB), that achieved direct treatment of real municipal wastewater, recovery of purified ammonium sulfate, and reuse of homogeneous catalysts. This study advances energy-efficient distributed ammonia production, and provides a tunable platform for molecular electrocatalysts to interface with wastewater treatment.

1. Introduction

Circular wastewater refining processes can responsibly manage aqueous waste streams and sustainably produce chemical commodities, including nitrogen compounds. Conventionally, nitrogenous commodities are produced from ammonia-nitrogen

made using the Haber–Bosch (HB) process; this process is highly energy-efficient but contributes 1–2% of global carbon dioxide emissions.¹ The majority of HB-nitrogen is used as fertilizer,² but 24–54% of HB-nitrogen is discharged from anthropogenic processes as aqueous nitrate (NO_3^-) and ammonium (NH_4^+).³ Excess reactive nitrogen species in surface waters cause algal blooms that damage aquatic ecosystems and exacerbate climate change.^{4–6} Refining these fugitive nitrogen emissions into a tunable, diverse portfolio of products could simultaneously remediate harmful pollutants and generate 19 billion USD annually.³ The electrocatalytic NO_3^- reduction reaction (NO_3RR) to ammonia can refine nitrate-rich wastewaters that contain 19–48 Tg NO_3^- –N globally per year.³ Electrified NO_3RR processes will readily integrate with renewable and decentralized energy sources, which could enable ammonia production at sites of

^a Department of Chemical Engineering, Stanford University, Stanford, CA, 94305, USA. E-mail: wtarpeh@stanford.edu; Tel: +1-650-497-1324

^b Department of Civil and Environmental Engineering, Stanford University, Stanford, CA, 94305, USA

^c Woods Institute for the Environment, Stanford University, Stanford, California, 94305, USA

† Electronic supplementary information (ESI) available: Supplementary Fig. S1–S39, Tables S1–S7, and eqn S3.1.1–S7.2.1. See DOI: <https://doi.org/10.1039/d4ee01727g>

wastewater generation. This circular NO_3^- refining paradigm can improve sanitation access, expand nitrogen commodity access, and offset costs and emissions of industrial ammonia production.

Despite the large overall flux of anthropogenic nitrogen discharges into the environment, most NO_3^- is contributed by dilute and impure wastewater sources.⁷ Both point sources (e.g., municipal wastewater) and nonpoint sources (e.g., agricultural runoff) generally contain less than 50 mg NO_3^- –N L⁻¹ (3.6 mM).^{8–13} Municipal and agricultural wastewaters are also impure; they contain co-constituents (e.g., organic/inorganic ions, organic carbon, suspended solids) that compete for catalyst active sites, degrade catalysts over time, passivate electrode surfaces, and alter solution pH outside of catalyst operating ranges.^{14–16} In contrast to real wastewaters, NO_3RR electrocatalysts are most heavily documented with NO_3^- concentrations above 100 mM (*i.e.*, concentrated) in synthetic (*i.e.*, pure) electrolytes.^{14,17–26} NO_3^- refining research must overcome the difference in the NO_3^- concentration and purity between catalysis investigations and real wastewaters to be relevant for wastewater treatment and chemical manufacturing.

Homogeneous molecular catalysts are promising for wastewater NO_3^- refining because their atomically precise reactivity could overcome both dilute and impure wastewater conditions;²⁷ however, these catalysts are rarely explored for wastewater treatment because they require separation. The ligand structures of molecular catalysts promote high reactant and product selectivities that could enhance NO_3RR faradaic efficiency (FE) and reaction rates to total ammonia nitrogen (TAN; the sum of NH_4^+ –N_(aq) and NH_3 –N_(aq)) in dilute NO_3^- solutions. The metal complex 2,3-dimethyl-1,4,8,11-tetraazacyclotetradeca-1,3-diene (DIM) with a Co metal center, abbreviated as Co(DIM), yields TAN as its major product and suppresses the competitive hydrogen evolution reaction (HER) under aqueous conditions from pH 3.5 to 10.1.²⁸ Co(DIM) is easily synthesized²⁹ and exemplifies untapped benefits to employing molecular electrocatalysts for wastewater refining. The positively charged metal center of Co(DIM) facilitates binding of negatively-charged NO_3^- .²⁸ Additionally, homogeneous electrocatalytic processes directly scale with volume³⁰ (e.g., Fenton catalysts,³¹ porphyrins for PFAS remediation³²) and can use economical carbonaceous electrode materials. Rational design principles for molecular electrocatalyst design, operation, and separation in wastewater refining processes are currently ill-defined because there are few use-informed investigations of homogeneous catalysis in real wastewaters contexts.

Likewise, rational design of wastewater refining unit processes is hampered by a dearth of electrochemical investigations that integrate reactions and separations, or reactive separations.^{3,33} Consequently, unit process performance (namely efficiencies, rates, and energy consumption) is difficult to benchmark against incumbent wastewater management processes. Reactive separations can overcome the challenges of dilute and impure wastewaters to enable NO_3^- extraction, NO_3^- conversion to TAN, and purified TAN recovery.^{3,33} However, there are few investigations of reactive separations in real wastewaters,^{34–36} and even fewer in dilute wastewaters.³⁷ Our recent work demonstrated that homogeneous electrocatalysis

in existing NO_3RR reactive separation architectures can produce purified TAN ($(\text{NH}_4)_2\text{SO}_4$ –N_(aq)).³⁸ Elevating this preliminary demonstration to rationally-designed unit processes requires investigation of interfacial phenomena imposed by catalytically influential wastewater species.^{16,33}

To address the rational design challenges imposed by dilute and impure NO_3^- , we investigated interfacial mechanisms that govern Co(DIM)-mediated NO_3RR reactive separations performance in real wastewaters, and leveraged these insights toward engineering novel molecular catalysis systems. The major contribution of this work was to develop and interrogate molecular catalysis systems capable of converting wastewater nitrate into high-purity ammonia; which was enabled by several key advances. First, investigating catalysis (*via* electrolysis, amperometry, and spectroscopy) in a systematic suite of simulated and real wastewater electrolytes elucidated the mechanistic influences of inorganic ions on reactor performance. More specifically, we investigated the effect of bulk and interfacial ionic composition on activity and FE, and found that magnesium ions play a deterministic role in electrode fouling. Second, these mechanistic insights enabled rational design of a novel reactive separations unit process, electrocatalyst-in-a-box (ECaB). Our first ECaB iteration (proof-of-concept ECaB) exhibited sustained activity, high FE, and low energy consumption for several cycles to treat a real, NO_3^- -bearing wastewater: municipal secondary effluent. Third, proof-of-concept ECaB enabled long-term evaluation and benchmarking of the full unit process and its subunit processes against related NO_3RR efforts and conventional nitrogen management (wastewater treatment and HB-ammonia production). Proof-of-concept ECaB also generated a high-purity TAN product with the lowest reported energy consumption ($90.0 \pm 2.7 \text{ kW h kg N}^{-1}$) for any NO_3RR reactive separation process to date. In a second, improved iteration (subunit engineered ECaB), we leveraged reactor design to improve subunit process rates toward scalable performance targets. Ultimately, our findings span from the microenvironment to the unit process scale and contribute to the informed design of catalysts, electrode and membrane interfaces, and electrochemical reactors. This study demonstrates a novel use-informed, iterative approach to wastewater electrocatalysis that guides the development of efficient and practical reactors for pollution remediation and circular chemical manufacturing.

2. Results & discussion

Because the primary NO_3^- -rich wastewaters are municipal secondary effluent and fertilizer runoff, NO_3RR processes must operate with feed compositions of dilute NO_3^- (<4 mM), low conductivity (<2 mS cm⁻¹), and water hardness (*i.e.*, presence of divalent metal cations).^{37,38} We collected and conducted experiments in a representative secondary effluent (Table S1, ESI[†]) containing 120 mg NO_3^- L⁻¹ (28 mg NO_3^- –N per L, 2.0 mM NO_3^-) and a matrix of anions, alkaline earth metal cations, suspended solids, and organic and inorganic carbon. Within this complex composition, we sought to uncover the

promoting or inhibiting effects of specific wastewater constituents on Co(DIM)-mediated NO_3RR (Section 2.1). Toward this goal, we assessed the NO_3RR performance as a function of electrolyte composition (Section 2.1.1) and described generalizable interfacial mechanisms that influence Co(DIM)-mediated NO_3RR behavior (Section 2.1.2). These insights informed the design and development of the novel reactive separations process ECaB (Section 2.2). Proof-of-concept ECaB (Section 2.2.1) demonstrated robust performance with real wastewater and enabled systematic comparisons to previous NO_3RR investigations (Section 2.2.2). Finally, subunit engineered ECaB demonstrated improved subunit process rates toward tractable performance targets (Section 2.2.3).

2.1. Effects of electrolyte composition on Co(DIM)-mediated NO_3RR

2.1.1. Effects of bulk electrolyte composition on the observed NO_3RR performance. Cyclic voltammetry (CV) and controlled-potential electrolysis (CPE) elucidated Co(DIM)-mediated NO_3RR catalytic activity and selectivity as a function of electrolyte composition. In Fig. 1a, the GC working electrode without Co(DIM) in solution is inactive for the NO_3RR (NaCl and NaCl + NaNO₃ curves). In the presence of Co(DIM), two reversible redox peaks exist, the first at $E_{1/2} = +0.24$ V vs. Ag/AgCl (putatively Co^{III/II} redox) and the second at $E_{1/2} = -1.00$ V vs. Ag/AgCl (putatively Co^{III/I} redox).²⁸ With both Co(DIM) and NO_3^- in solution, catalysis is evidenced by an increased current density (*i.e.*, catalytic current) of the second reductive wave and loss of reversibility on the reverse (anodic) scan. Catalytic current is caused by local enrichment of [Co(DIM)] during heterogeneous activation and a homogeneous NO_3RR in the reaction-diffusion layer (RDL).³⁹ With higher Co(DIM) concentration (*i.e.*, lower excess factor), the

second reduction peak current increases linearly both in the presence and absence of NO_3^- . Prior work showed that the rate of homogeneous Co(DIM)-mediated NO_3RR is independent of pH and is first order with respect to [Co(DIM)] (0.5–5 mM) and $[\text{NO}_3^-]$ (5–100 mM).²⁸ Fig. 1b shows that homogeneous NO_3RR catalysis is first order with respect to [Co(DIM)] even at low excess factors (excess factor = $[\text{NO}_3^-]/[\text{Co(DIM)}]$) than tested previously (*i.e.*, <2), indicating catalysis outpaces bulk-phase catalyst diffusion. Additionally, the catalytic waveforms of 8 mM Co(DIM) are effectively identical in synthetic electrolyte (6.2 mM NaCl + 2 mM NaNO₃) and in real wastewater (Fig. S5, ESI†) at 100 mV s⁻¹, implying intrinsic catalytic activity is unaffected by complex wastewater electrolyte. This conclusion was tested in two-chamber CPE experiments with three catholytes (Table S1, ESI†). The sum of NO_3^- -N and TAN mass (Fig. 2a) remained near unity for all catholytes (97.7 ± 10.0% for simplified, 100.8 ± 4.7% for simulated, and 97.0 ± 4.8% for real wastewater). TAN selectivity (93.8 ± 7.3% for simplified, 106.5 ± 1.6% for simulated, and 79.5 ± 16.1% for real wastewater) and FE (41.4 ± 2.4% for simplified, 41.2 ± 1.6% for simulated, and 43.1 ± 7.0% for real wastewater) remained relatively unaffected by electrolyte composition (Section S3.1, ESI†); neither the difference between simplified and simulated CPEs ($p = 0.13 > 0.05$ for selectivity, $p = 0.17 > 0.05$ for FE) nor the difference between simplified and real CPEs ($p = 0.14 > 0.05$ for selectivity, $p = 0.62 > 0.05$ for FE) were statistically significant (Fig. 2b). Co(DIM) therefore enabled selective NO_3RR to TAN under all dilute NO_3^- conditions. However, NO_3^- conversion was significantly lower in simulated (12.4 ± 1.0%, $p = 0.029 < 0.05$) and real (10.3 ± 3.1%, $p = 0.0083 < 0.05$) wastewaters compared to simplified wastewater (32.6 ± 6.1%). Simulated wastewater was also a high-fidelity proxy of real wastewater, as demonstrated by the lack of significant

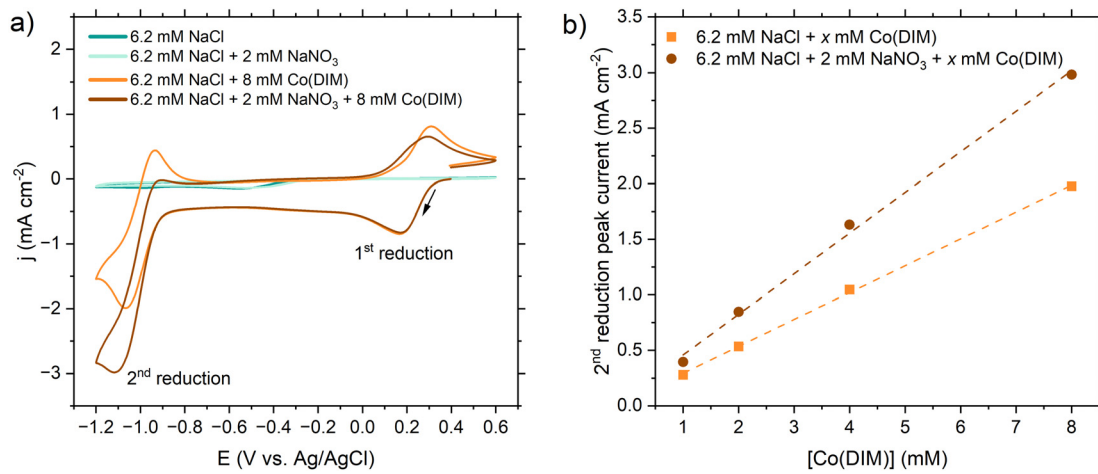


Fig. 1 (a) Cyclic voltammograms collected in 6.2 mM NaCl (background electrolyte matching the Cl^- concentration in real wastewater), 6.2 mM NaCl with 2 mM NaNO₃ (background electrolyte with representative nitrate concentration), 6.2 mM NaCl with 8 mM Co(DIM) (background electrolyte with catalyst), and 6.2 mM NaCl with 2 mM NaNO₃ and 8 mM Co(DIM) (background electrolyte with catalyst and representative nitrate concentrations). Working electrode: 5 mm GC disk. Counter electrode: 6.4 mm graphite rod. Reference electrode: Ag/AgCl (4.0 M KCl). Scan rate: 100 mV s⁻¹. (b) Peak current density of the second reduction peak (~ -1.1 V vs. Ag/AgCl) of 6.2 mM NaCl with 8 mM Co(DIM) in the presence and absence of 2 mM NaNO₃. Associated voltammograms are provided in Fig. S4 (ESI†). The excess factor, defined as the concentration of substrate (NO_3^-) divided by the concentration of catalyst (Co(DIM)), ranged from 2 to 200 previously. To address dilute real wastewaters, we minimized the excess factor with 8 mM Co(DIM) (the observed solubility limit at room temperature) to maximize NO_3RR activity (excess factor = 0.25, Fig. 1b).

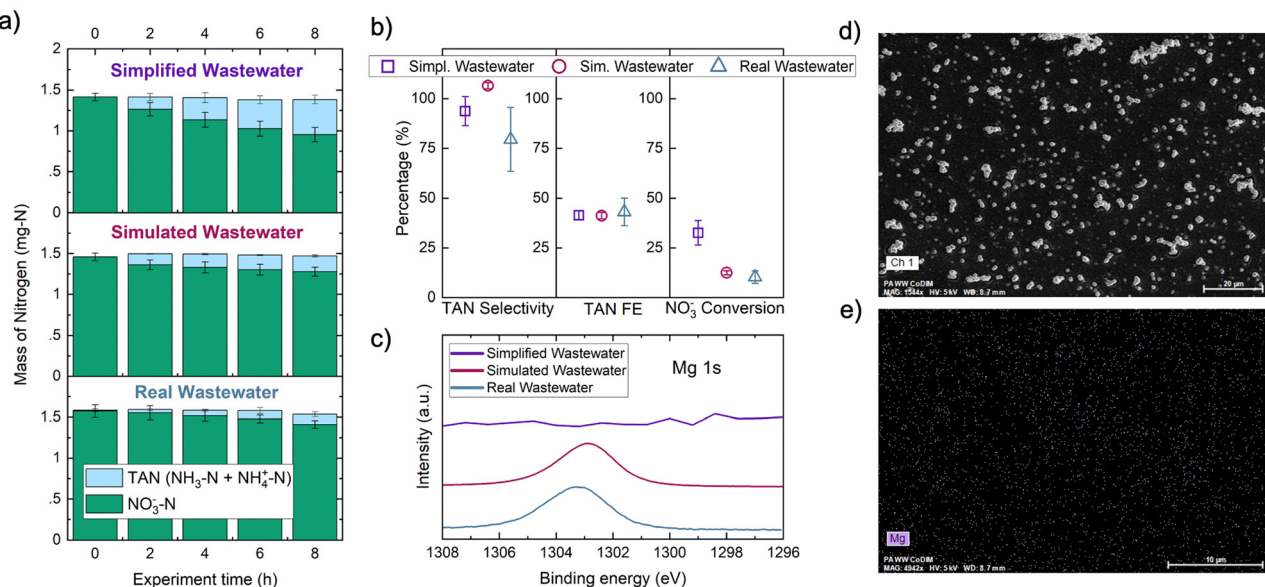


Fig. 2 (a) Mass balance of aqueous nitrogen species as a function of time during two-chamber controlled-potential electrolysis (CPE) experiments at -1.05 V vs. Ag/AgCl performed in three electrolytes: 8 mM Co(DIM) in simplified wastewater, 8 mM Co(DIM) in simulated wastewater, and 8 mM Co(DIM) in real wastewater. Error bars represent \pm one standard deviation from triplicate experiments ($n = 3$). For all three electrolytes, NO₃⁻-N and TAN closed the nitrogen mass balance within $\pm 3\%$. No TAN was detected after CPE without NO₃⁻ (Fig. S6, ESI†), confirming that the measured TAN was the result of the NO₃RR. The closed mass balance and catalytic TAN formation support for NO₃RR selectivity to TAN remained near 100% in all three electrolytes tested, consistent with previous investigations.^{28,38} (b) Cumulative TAN selectivity, TAN faradaic efficiency, and NO₃⁻ conversion for 8 hour CPE experiments. (c) Mg 1s XPS spectra of the glassy carbon plate cathode after CPE experiments. After CPE the electrode was rinsed with nanopure water and blow dried with N₂ before XPS and SEM-EDS analysis. (d) SEM image and (e) Mg EDS map of the glassy carbon plate cathode after a CPE experiment in real wastewater, showing dispersed deposits of Mg on the surface.

difference in conversion between these two streams ($p = 0.31 > 0.05$). Therefore, inorganic ionic constituents in the wastewater matrix were most responsible for inhibiting catalyst activity.

Whereas NO₃RR activity was strongly influenced by wastewater impurities, the relatively low FE_{TAN} was primarily influenced by NO₃⁻ concentration. Under purely kinetic conditions,³⁹ Co(DIM)-mediated NO₃RR is first order in [Co(DIM)] and [NO₃⁻], motivating the high catalyst concentrations employed in CVs and CPEs. However, purely kinetic conditions do not apply in our CPE experiments because the low excess factor imposed by the wastewater caused substrate consumption in the RDL, and consequently a significant amount of current was consumed by non-catalytic reductions of Co(DIM). Several control CPE experiments were performed to quantify non-catalytic charge allocation (*i.e.*, FE). CPE at -0.75 V_{Ag/AgCl} (-0.99 V vs. first reduction, $+0.25$ V vs. second reduction) in simplified wastewater (6.2 mM NaCl + 2 mM NaNO₃) served as a proxy for non-catalytic charge toward the first reduction of Co(DIM); CPE at -1.05 V_{Ag/AgCl} in a modified simplified wastewater (6.2 mM NaCl + 0 mM NaNO₃) served as a proxy for non-catalytic charge toward the first and second reductions. The sum of charge associated with non-catalytic reductions of Co(DIM) accounts for 89.4% of charge passed in the simplified wastewater CPEs (Fig. S6 and S7, ESI†), reasonably closing the balance of FE. Notably, the non-catalytic charge passed (49.3% FE) exceeded the catalytic charge passed (41.4 \pm 2.4% FE). The excess factor therefore significantly influences the ratio of activated Co(DIM) molecules that successfully perform NO₃RR in the homogeneous phase.

Because only NO₃⁻ conversion was significantly changed as a function of electrolyte composition, we hypothesized that electrode fouling in simulated and real wastewater reduced the observed NO₃RR rate by impeding Co(DIM) activation at the heterogeneous electrode-electrolyte interface. Visible deposits were present on the electrode after 8 hours for all three electrolytes (Fig. S8, ESI†), prompting spectroscopic and electrochemical characterization of the GC surface. Based on simulated wastewater exhibiting electrode fouling, we expected that hardness (*e.g.*, Mg²⁺, Ca²⁺) and HCO₃⁻/CO₃²⁻ ions were precipitate components. XPS (Fig. 2c) and SEM/EDS (Fig. 2d and e) revealed magnesium on the GC surface for real and simulated wastewater. The pH required for precipitation of Mg(OH)₂ from 1.5 mM Mg²⁺ is 9.8 (Table S2, ESI†). Because the bulk pH of all three catholytes remained below 9.8 (Fig. S9, ESI†), the interfacial pH in the RDL likely exceeded pH 9.8, which is common under reducing electrochemical conditions.⁴⁰ No significant precipitation of Ca²⁺ was observed by EDS after real wastewater CPE (Fig. S10 and S11, ESI†), implying that the interface remained below pH 12.8 which is required to precipitate Ca(OH)₂ from 1.9 mM Ca²⁺. We also compared the catalytic activity and charge transfer resistance of the deposits formed on GC cathodes in simplified and real wastewaters. In rinse tests, both deposits were less active than homogeneous Co(DIM) and were not selective for TAN or NO₂⁻ (Fig. S12 and S13, ESI†). Thus, we did not consider the Mg-containing deposits to be catalytic for NO₃RR. The charge transfer resistance between the electrode surface and homogeneous Co(DIM) at the open circuit

potential (OCP) was greater for the real deposit ($R_{ct} = 310 \text{ k}\Omega$) than for the simplified deposit ($R_{ct} = 189.4 \text{ k}\Omega$) and the pristine GC surface ($R_{ct} = 132.7 \text{ k}\Omega$) (Fig. S14, ESI[†]). In conjunction with the insensitivity of TAN FE and selectivity to electrolyte composition (Fig. 2b), greater charge transfer resistance suggested that catalysis was heterogeneously inhibited by Mg deposition and that the homogeneous Co(DIM)-mediated NO_3^{RR} mechanism was unaffected by real wastewater impurities.

2.1.2. Interfacial mechanism of catalysis inhibition by Mg^{2+} . To identify specific inhibiting species, we dosed a small volume (28–38 μL , matching real wastewater concentrations, Table S1, ESI[†]) of 1 M solutions (MgCl_2 , CaCl_2 , and NaHCO_3) into simplified wastewater electrolyte with 8 mM Co(DIM) (Fig. 3a). The current density remained unchanged for all dosed species during uninterrupted RDE CPE experiments (green trace), contrary to the RDE CPE in real wastewater showing a distinct decay in current density (Fig. S15, ESI[†]). However, introducing an open circuit potential (OCP; purple trace) period caused a decay in current density for the Mg^{2+} dose experiment, but not for Ca^{2+} or HCO_3^- . XPS detected Mg deposits on the GC surface with an OCP period but not for uninterrupted CPE (Fig. 3b), further highlighting Mg^{2+} as the major foulant responsible for catalysis inhibition. If Mg^{2+} is homogeneously dispersed throughout the electrolyte when CPE begins (the case

for CPE after an OCP period), Mg^{2+} can specifically adsorb to the GC cathode. When the pH conditions for precipitation are met in the RDL, adsorbed Mg^{2+} ions form Mg deposits (most likely $\text{Mg}(\text{OH})_2$ based on the solubility product quotient, Q_{sp} , *versus* the solubility product constant, K_{sp} ; Table S2, ESI[†]), passivating the electrode. Conversely, if the RDL is established prior to introducing Mg^{2+} (the case for uninterrupted CPEs), positively-charged Co(DIM) in the RDL electrostatically and/or sterically impedes specific adsorption of Mg^{2+} . Thus, even if the pH conditions for precipitation are met in the RDL, repulsive interactions between Co(DIM) and Mg^{2+} may preclude precipitation and passivation for minutes to hours. To further confirm the role of Mg^{2+} , we demonstrated prolonged passivation in two ways. First, a longer CPE following Mg^{2+} in RDE (Fig. S16, ESI[†]) showed no change in current density over 40 min but showed an immediate decay in current density after an OCP period. Second, two-chamber CPEs for 8 hours (same two-chamber CPE setup as in Fig. 1; closed nitrogen mass balances in Fig. S17–S20, ESI[†]) with contaminant doses showed <6.3% change in NO_3^- conversion and TAN production (Fig. S21, ESI[†]). Thus activity, selectivity, and FE are unaffected by Mg^{2+} , Ca^{2+} , and HCO_3^- doses when Co(DIM) protects against passivation.

Magnesium precipitation during the Co(DIM)-mediated electrocatalytic NO_3^{RR} is generalizable to reductive homogeneous

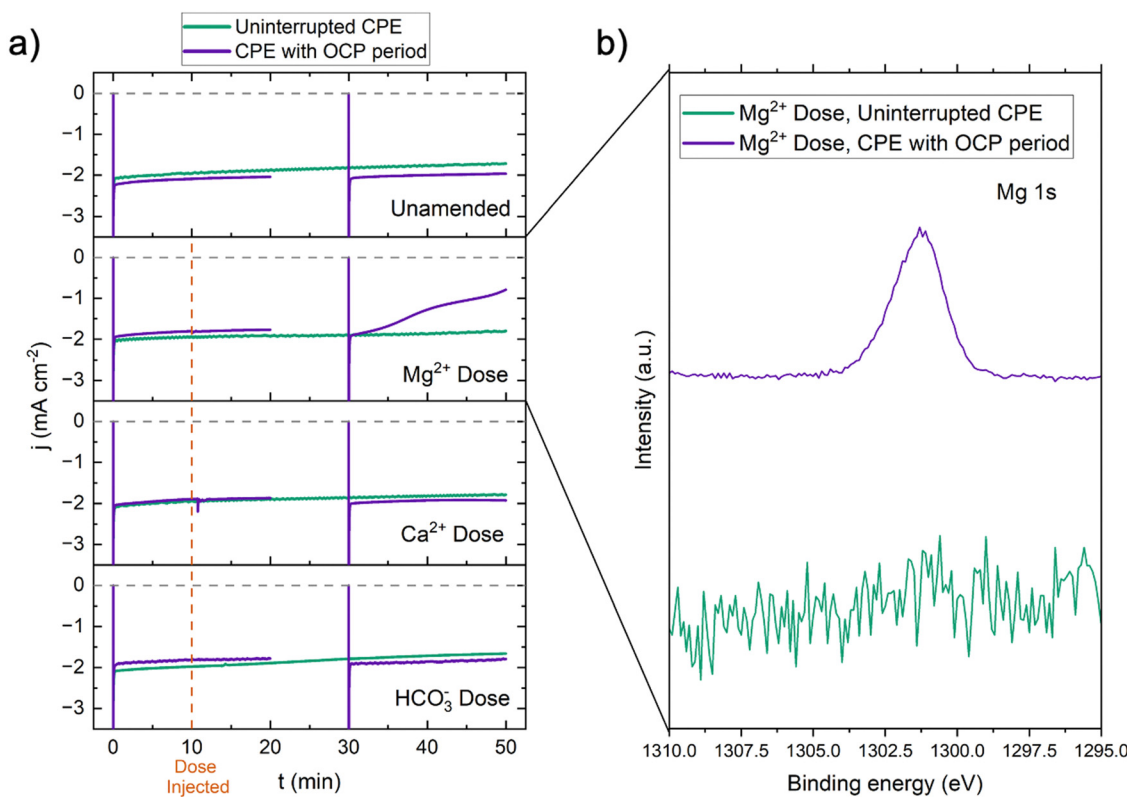


Fig. 3 (a) Current density vs. time of RDE CPEs $-1.05 \text{ V}_{\text{Ag}/\text{AgCl}}$ with suspected foulants manually dosed into the electrolyte at $t = 10 \text{ min}$ (no contaminant dose, 28 μL 1 M MgCl_2 , 30 μL 1 M NaHCO_3 , 38 μL 1 M CaCl_2). Two experiment conditions were compared: the first experiment held $-1.05 \text{ V}_{\text{Ag}/\text{AgCl}}$ for the full 50 minutes (green trace), and the second experiment introduced a period of open circuit potential (OCP) from $t = 20 \text{ min}$ to $t = 30 \text{ min}$. The counter electrode was a 6.4 mm graphite rod and the reference electrode was a Ag/AgCl (4.0 M KCl) electrode. The RDE was operated at 25 rotations per minute (RPM) because both catalytic current (for simplified wastewater) and inhibition (for real wastewater) were observed at this rotation rate (Section S4.1 and Fig. S15, ESI[†]). (b) Mg 1s XPS of the glassy carbon RDE electrode post Mg^{2+} dose CPE for both the uninterrupted CPE and the CPE with OCP period.

electrocatalysis and to the NO_3RR (heterogeneous or homogeneous) in real wastewaters. Similar precipitation processes have been observed in homogeneous CO_2 reduction electrocatalysis,⁴¹ and water hardness (*i.e.*, Mg^{2+} , Ca^{2+}) has been shown to decrease heterogeneous NO_3^- removal.¹⁶ In the secondary effluent used in this work (1.5 mM Mg^{2+}), a negligible proportion of Mg^{2+} present was consumed to form a passivating cathode deposit (Fig. S22, ESI†). Other nitrate-rich wastewaters like polluted groundwaters, reverse osmosis brines, and ion exchange brines may contain higher Mg^{2+} concentrations (up to 84 mM),⁴² increasing the likelihood of forming precipitates. Mg^{2+} electrode fouling is likely a widespread barrier to implementation. A reactive separation system could conceivably perform uninhibited NO_3RR directly in the native wastewater if divalent cations are repelled by near-surface confined Co(DIM) molecules. This insight motivates repulsive moieties at the electrode–electrolyte interface as a design principle for the microenvironment of homogeneous and heterogeneous catalyst systems. Electrode and catalyst design (*e.g.*, heterogeneous molecular catalysts, single-atom catalysts, ionomer coatings) could protect the cathode from passivation, but would not address the low TAN FE induced by inherently low NO_3^- concentrations in real wastewaters. The remainder of this study addresses cathode protection and FE_{TAN} with reactive separations that selectively extract and up-concentrate NO_3^- (and reject Mg^{2+}) from wastewater before catalysis.

2.2. Electrocatalyst-in-a-box (ECaB)

We mitigated cathode passivation in the NO_3RR by pre-catalysis extraction of NO_3^- from wastewater *via* reactive separations. Extracting NO_3^- into a synthetic electrolyte for Co(DIM)-mediated NO_3RR could be achieved by electrochemical separations such as electrodialysis,⁴³ capacitive deionization,⁴⁴ or electrosorption,³⁷ but in low-conductivity NO_3^- -rich wastewaters, electrochemical extraction can dominate the total process energy consumption.^{33,37} This observation motivates low-energy extraction methods like Donnan membrane dialysis.⁴⁵ Because Donnan equilibrium conditions are governed by electrochemical potentials (not concentrations) across the membrane, NO_3^- ions can diffuse against their concentration gradient by exchanging with high-activity receiver solution anions (*e.g.*, Cl^-). If the receiver solution volume is less than the feed solution (wastewater) volume, NO_3^- in the receiver solution can be substantially up-concentrated relative to the feed concentration. The resulting receiver solution is an ideal electrolyte for the NO_3RR because of its high conductivity, high NO_3^- concentration, and absence of Mg^{2+} . Donnan dialysis (DD) can also obviate separations challenges imposed by complex electrolyte compositions (*e.g.*, high $[\text{Cl}^-]$, divalent ions, organics), like unselective ion extraction, high energy consumption, and high capital costs.⁴⁵ In this section, we report a combined DD, NO_3RR , and ammonia stripping system coined electrocatalyst-in-a-box (ECaB; Fig. 4a).

2.2.1. Proof-of-concept ECaB with real wastewater. The ECaB unit process performs three subunit processes—wastewater NO_3^- extraction, NO_3^- conversion to TAN, and TAN

recovery—in a configuration of four electrolyte reservoirs (wastewater, catholyte, anolyte, and trap) and two applied potential conditions (OCP and $-1.05 \text{ V}_{\text{Ag}/\text{AgCl}}$). First, DD facilitates wastewater NO_3^- extraction *via* ion exchange with catholyte Cl^- ions across an AEM. To up-concentrate the catholyte NO_3^- , we used four times as much municipal secondary effluent volume (200 mL) as catholyte volume (50 mL). In proof-of-concept ECaB experiments (Fig. 4b), the catholyte NO_3^- was up-concentrated by 2.9 times from $27.8 \pm 0.5 \text{ mg N per L}$ ($2.0 \pm 0.04 \text{ mM}$) to $80.8 \pm 2.8 \text{ mg N per L}$ ($5.8 \pm 0.2 \text{ mM}$) over the first 24 h OCP period when only DD was active. Meanwhile, the wastewater NO_3^- concentration decreased to $5.0 \pm 0.9 \text{ mg N per L}$ ($0.36 \pm 0.06 \text{ mM}$), below the drinking water standard of 10 mg N per L,⁴⁶ at a NO_3^- removal rate ($7.8 \pm 0.1 \text{ mg NO}_3^- \text{ N L}^{-1} \text{ day}^{-1}$) that exceeds conventional wastewater treatment (*i.e.*, nitrification–denitrification; $\sim 5 \text{ mg NO}_3^- \text{ N L}^{-1} \text{ day}^{-1}$).⁴⁷ DD requires no electrochemical energy input to extract and up-concentrate NO_3^- in the catholyte, only the embedded energy requirement to produce NaCl. DD paired with the NO_3RR therefore subverts the energy consumption-reaction rate tradeoff in NO_3RR reactive separations. At 24 h, $-1.05 \text{ V}_{\text{Ag}/\text{AgCl}}$ was applied to stimulate Co(DIM)-mediated NO_3RR (24–34 h), corresponding to a decrease in catholyte NO_3^- and an increase in catholyte TAN. $-1.05 \text{ V}_{\text{Ag}/\text{AgCl}}$ was held for 10 h periods to keep Co(DIM) in its stable operating pH regime;^{28,38} operation for longer than 10 h in these experiments resulted in catholyte pH > 11 and a significant decrease in FE_{TAN} . After 6 h of CPE, the catholyte pH (Fig. S23, ESI†) was sufficiently alkaline for catholyte TAN to exist primarily as NH_3 ($\text{pK}_{\text{aNH}_4^+/\text{NH}_3} = 9.25$), which volatilized, crossed the GPM, and was recovered in the acid trap (0.1 M H_2SO_4). ECaB was recirculated overnight (34–48 h) at open circuit as the remaining TAN migrated across the GPM. At 48 h, the catholyte was adjusted back to pH 6 with $\sim 200 \mu\text{L}$ 10 wt% HCl to keep Co(DIM) in its stable operating pH regime^{28,38} before a second cycle of CPE (48–58 h) and OCP (58–72 h) began. ECaB experiments were performed for three cycles for a total of 96 h (30 cumulative hours of CPE) to demonstrate proof-of-concept. The total measured N masses (Fig. 4c) at 24 h, 48 h, 72 h, and 96 h accounted for $97.6 \pm 1.4\%$, $88.7 \pm 5.1\%$, $84.1 \pm 2.7\%$, and $84.9 \pm 1.8\%$ of the influent wastewater $\text{NO}_3^- \text{ N}$. We hypothesize that binding of NH_3 to Co(DIM) was the largest contributor to unclosed mass balances because the largest changes occurred during recirculation at OCP from 34–48 h and Co(DIM) in its Co(III) oxidation has a high NH_3 binding capacity (at least 1.6 mM TAN/mM Co(DIM); Fig. S24, ESI†). Unlike many electrolysis approaches, the wastewater remained circumneutral for the duration of experiments ($\text{pH } 7.07 \pm 0.25$ at $t = 96 \text{ h}$, Fig. S23, ESI†), demonstrating potential for downstream water reuse. Combining membrane-based DD and ammonia stripping isolates the homogeneous Co(DIM) solution from the wastewater feed and the TAN product (Fig. S25, ESI†), enabling treated wastewater recovery, product TAN recovery, and homogeneous catalyst reuse. This catalyst reuse is similar to catalyst-in-a-cup⁴⁸ (in which thermal homogenous catalysts are separated from solvents, reactants, and products in chemical production), inspiring the ECaB name.

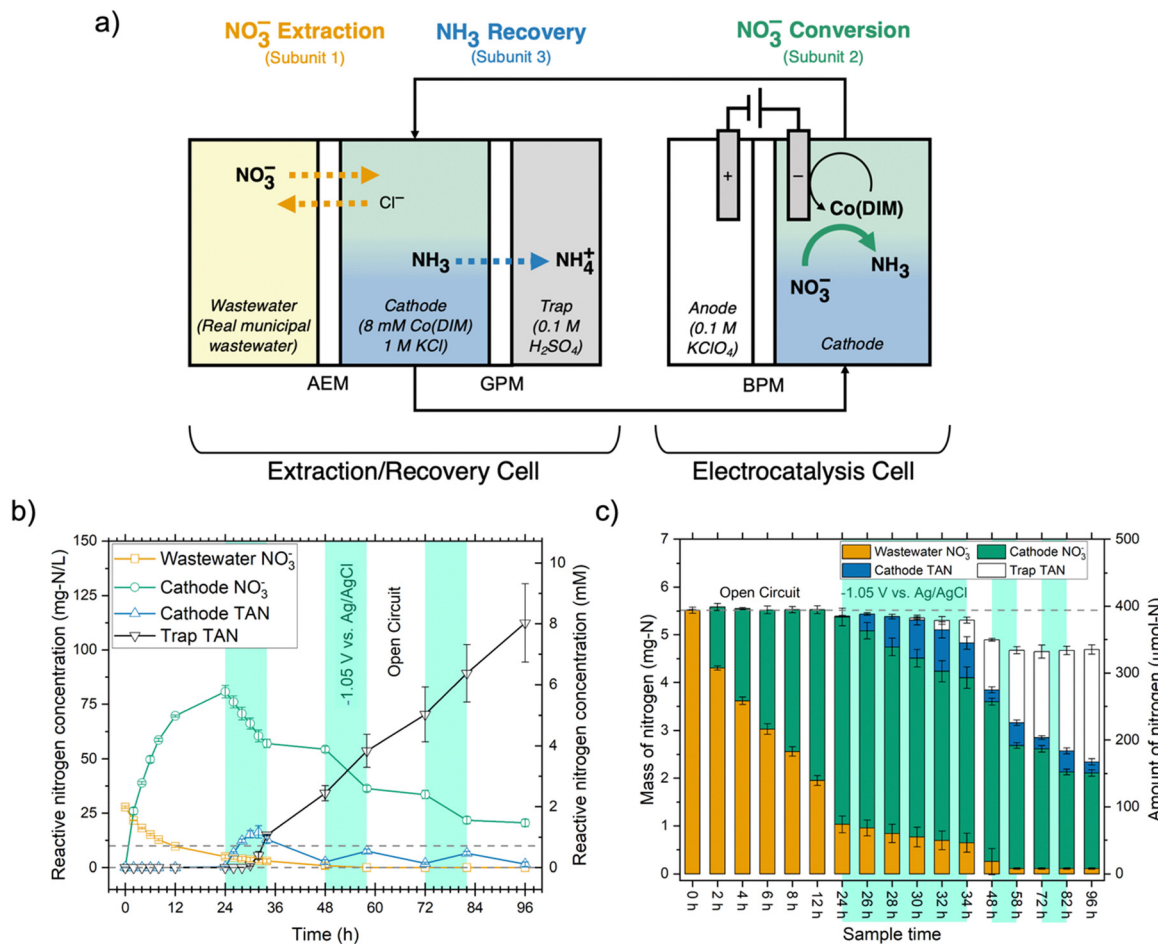


Fig. 4 (a) Electrocatalyst-in-a-box (ECaB) schematic. Wastewater-NO₃⁻ extraction (subunit process 1, orange) is achieved by Donnan dialysis (DD) in the extraction/recovery cell (left) where NO₃⁻ ions exchange with Cl⁻ ions due to an electrochemical potential gradient across the anion exchange membrane (AEM). The catholyte recirculates between the extraction/recovery cell and the bipolar membrane (BPM)-separated electrocatalysis cell (right) where Co(DIM)-mediated NO₃RR (subunit process 2, green) converts NO₃⁻ to TAN. As the catholyte basifies under reducing conditions, the majority of TAN exists as NH₃ that is recovered (subunit process 3, blue) by diffusing across the gas-permeable membrane (GPM) into the acidic trap chamber. (b) NO₃⁻ and TAN concentrations and (c) nitrogen mass balance for electrocatalyst-in-a-box experiments. Error bars represent \pm one standard deviation from triplicate experiments ($n = 3$). Detailed experimental parameters of ECaB tests can be found in the Methods section 4.2.3. Time periods where the electrochemical cell was held at open circuit (OCP; 0–24 h, 34–48 h, 58–72 h, 82–96 h) are indicated by a white background and time periods where the electrochemical cell was held at -1.05 V_{Ag/AgCl} (24–34 h, 48–58 h, 72–82 h) are indicated by a green background. Applied potentials were held for 10 h at a time to keep Co(DIM) in its stable operating pH regime.^{28,38} The dashed line in panel (b) indicates the drinking water limit of 10 mg NO₃-N per L.

2.2.2. Reactive separation unit and subunit process performance metrics. By decomposing the NO₃⁻ refining process into subunit processes (NO₃⁻ extraction, NO₃⁻ conversion, and TAN recovery), ECaB facilitates systematic comparisons of NO₃⁻ refining studies in terms of efficiencies, rates, and energy consumption (Tables S4–S7, ESI[†]).⁴⁹ The overall nitrogen recovery efficiency ($\eta_{\text{Overall N recovery}} = \frac{\text{mol N}_{\text{recovered}}(t)}{\text{mol N}_{\text{wastewater}}(\text{initial})}$) is the product of NO₃⁻ extraction efficiency, TAN yield, and TAN recovery efficiency (Section S5.1 and Fig. S26, ESI[†]). For ECaB, $98.1 \pm 0.3\%$ of wastewater NO₃⁻ was extracted by the end of the 96 h experiments, with $81.3 \pm 3.3\%$ extracted in the first 24 hours (Fig. 5a). $60.8 \pm 1.1\%$ of extracted NO₃⁻ was converted via Co(DIM)-mediated NO₃RR and $91.0 \pm 2.1\%$ of the produced TAN was recovered in the trap. Overall, $42.6 \pm 1.4\%$ of influent wastewater NO₃⁻-N was recovered as TAN. Proof-of-concept ECaB prevented

cathode Mg fouling and enabled sustained NO₃⁻ conversion via selective NO₃⁻ extraction (Fig. S27–S29, ESI[†]). Despite having a more complex composition, ECaB with real wastewater outperformed CPE in simplified wastewater in terms of FE_{TAN} (Fig. 5b) and NO₃⁻ conversion rate (Fig. 5c). Additionally, Mg²⁺ was not detected in the catholyte nor on the GC surface by XPS (Fig. S30, ESI[†]) or EDS (Fig. S31, ESI[†]), reinforcing that Co(DIM)-mediated NO₃RR activity in ECaB was not inhibited by cathode passivation. ECaB exemplifies a reactive separation process for treating real wastewater, and outperforms a simplified (*i.e.*, ideal) system driven by insights into wastewater-induced inhibition.

Proof-of-concept ECaB recovered a pure (NH₄)₂SO₄ with record low energy consumption (90.0 ± 2.7 kW h kg N⁻¹) for a NO₃RR reactive separation process (Fig. 6), due to the selectivity and FE_{TAN} of Co(DIM)-mediated NO₃RR in relatively dilute NO₃⁻ ($\leq 5.8 \pm 0.2$ mM for all time points). Energy

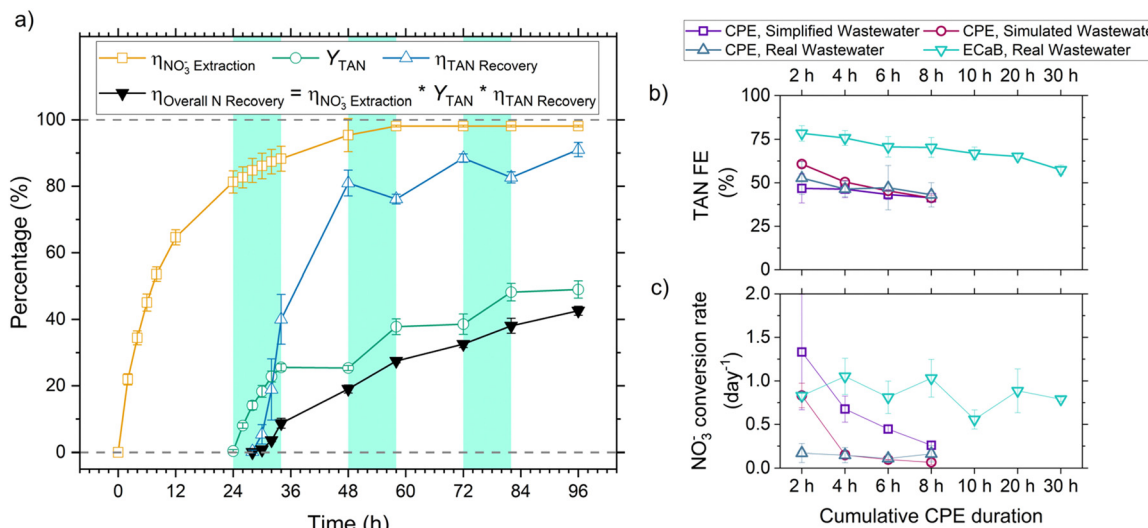


Fig. 5 (a) Cumulative NO_3^- extraction efficiency ($\eta_{\text{NO}_3^- \text{ extraction}}$), TAN yield (Y_{TAN}), TAN recovery efficiency ($\eta_{\text{TAN recovery}}$), and overall nitrogen recovery efficiency ($\eta_{\text{Overall N recovery}}$) during ECaB experiments. Error bars represent \pm one standard deviation from triplicate experiments ($n = 3$). Detailed experimental parameters of ECaB tests can be found in the Materials & methods section 4.2.3. Time periods where the electrochemical cell was held at open circuit (OCP; 0–24 h, 34–48 h, 58–72 h, 82–96 h) are indicated by a white background and time periods where the electrochemical cell was held at $-1.05 \text{ V}_{\text{Ag}/\text{AgCl}}$ (24–34 h, 48–58 h, 72–82 h) are indicated by a green background. (b) Cumulative FE_{TAN} as a function of cumulative CPE duration. (c) Pseudo-instantaneous NO_3^- conversion rate (nitrate converted over one sample period divided by the preceding sample period nitrate concentration; eqn (S5.1.16), ESI†). Equations used to calculate efficiency and rate metrics can be found in Section S5.1 (ESI†).

consumption is a major driver of wastewater treatment technology feasibility⁴⁹ and is therefore a crucial metric to compare to related systems and to incumbent processes. Proof-of-concept ECaB demonstrates that its subunits (NO_3^- extraction, NO_3^- conversion, and TAN recovery; Fig. 6 symbol shape) consume a proportionate amount of energy in an integrated unit process format. The cumulative energy consumption was also achieved from real wastewater using reactive separations, demonstrating robust process capabilities (Fig. 6 symbol color). The cumulative energy consumption of proof-of-concept ECaB is within 3.6–7.1 times that of conventional centralized nitrogen management (12.7–25.1 kW h kg N^{-1}), consisting of HB ammonia production (7.7–10.1 kW h kg N^{-1})⁵⁰ and nitrification-denitrification (NDN) wastewater treatment (5–15 kW h kg N^{-1}).⁵¹ Additionally, the cost of producing ammonium sulfate in ECaB is \$2.70 kg N^{-1} and competitive with the retail price (\$2.89 kg N^{-1}) if electricity is considered the only operational expenditure (Section S5.1, ESI†).⁵² The low energy consumption and product cost in proof-of-concept ECaB are promising, but the long operational timescale (96 h) is limited by the relatively slow NO_3^- conversion subunit rate (Fig. S32, ESI†).

2.2.3. ECaB subunit process engineering. Because the ECaB subunit processes rely on preceding subunits, the rate-limiting NO_3^- conversion subunit was improved by process engineering of the preceding NO_3^- extraction step. DD equilibrium calculations suggested that catholyte $[\text{NO}_3^-]$ up-concentration could exceed 100 \times compared with our 2 mM wastewater NO_3^- feed solution (Fig. S33, ESI†). In subunit engineered ECaB experiments, we used a commercial electrolyzer with a serpentine flow field to minimize solution-phase mass transport limitations (Fig. S34 and S35, ESI†). This modification enabled NO_3^- extraction

in subunit engineered ECaB to treat 10 \times the volume of wastewater compared to the proof-of-concept (Section 2.2.1) to below the drinking water $[\text{NO}_3^-]$ limit in the same 24 h period (67.5% of NO_3^- extracted; Fig. S36 and S37, ESI†). The corresponding subunit engineered NO_3^- extraction rate (151.6 $\mu\text{g N cm}^{-2} \text{h}^{-1}$) was 14.6 \times that of the proof-of-concept (Table 1, Fig. S38, ESI†). The resulting up-concentrated catholyte $[\text{NO}_3^-]$ was 54.4 mM, which improved the NO_3^- conversion subunit by Co(DIM)-mediated NO_3^- RR's first order dependence on $[\text{NO}_3^-]$. Subunit engineered ECaB achieved a TAN partial current density (j_{TAN}) of 5.1 mA cm^{-2} (319.6 $\mu\text{g N cm}^{-2} \text{h}^{-1}$): 20.4 \times that of the proof-of-concept. The improved j_{TAN} enabled a TAN yield of 82.5% in only 8 h. Though we made no modifications to the TAN recovery subunit, the TAN recovery rate was 7.6 \times that of the proof-of-concept due to an increased TAN concentration gradient from catholyte to trap; we hypothesize that mass transport enhancements can further improve TAN recovery rate. The subunit engineered ECaB energy consumption for TAN production (67.2 kW h kg N^{-1}) is even lower than proof-of-concept ECaB (81.9 \pm 3.5 kW h kg N^{-1} , Fig. S38, ESI†). We thus overcame ECaB rate limitations by subunit process engineering while maintaining the proof-of-concept process innovations (low energy consumption and Mg fouling prevention).

To quantify the performance gap between subunit engineered ECaB and operationally feasible systems, we derived scenario-based j_{TAN} targets from a cost assessment of wastewater treatment coupled with fertilizer production. Cost was chosen as a basis for targets because it is the largest driver of wastewater treatment technology feasibility;⁴⁹ j_{TAN} was chosen as a representative performance target because it influences cost^{57,58} and facilitates comparisons across electrochemical

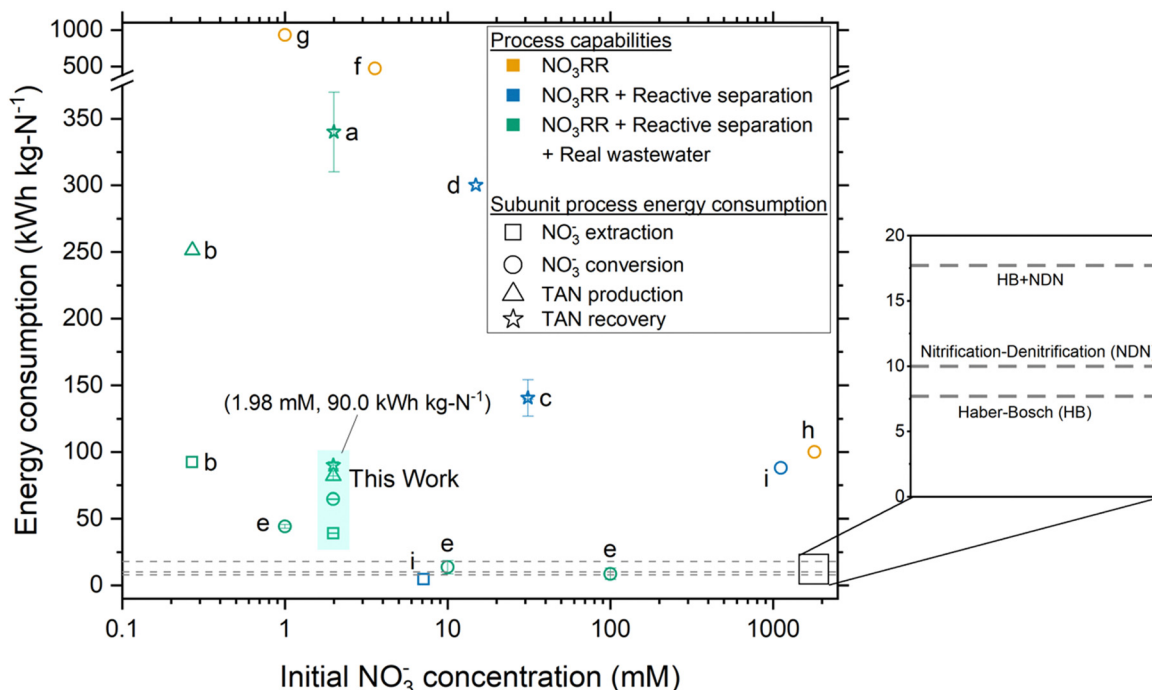


Fig. 6 Energy consumption of NO_3^- extraction, NO_3^- conversion, TAN production, and TAN recovery subunit processes for reports of reactive separations in NO_3RR literature. Error bars for this work represent \pm one standard deviation from triplicate experiments ($n = 3$). Error bars were included as-reported for references a, c, and e. Fig. 6 shows ECaB energy consumption (kWh kg N^{-1}) where the numerator is the same energy for all metrics and the denominator is the nitrogen mass associated with NO_3^- extraction, NO_3^- conversion, TAN production, and TAN recovery (Section S5.1, ESI†). Energy consumption values shown are therefore cumulative, such that a subunit process energy consumption is the sum of all preceding subunit processes (i.e., TAN recovery will always be the largest because it is the sum of all subunit processes). Equations used to calculate energy consumption are detailed in Section S5.1 (ESI†). For proof-of-concept ECaB, NO_3^- extraction and TAN recovery do not explicitly consume energy but are calculated as non-zero values here as the electrochemical energy consumed divided by the mass of nitrogen extracted or recovered, respectively. References for reported values from NO_3RR studies in the literature are as follows: a,³⁸ b,³⁷ c,³⁴ d,³⁵ e,⁵³ f,⁵⁴ g,⁵⁵ and h.⁵⁶ Note that studies e, f, and g were focused on the removal of NO_3^- as N_2 . Tables S4–S7 (ESI†) provide a detailed comparison of ECaB to the NO_3RR systems referenced in Fig. 6. The dashed lines indicate the energy consumption of Haber–Bosch (HB), nitrification–denitrification (NDN), and the summed energy consumption of HB + NDN.

Table 1 Summary of performance metrics for the proof-of-concept and subunit engineered ECaB iterations

Metric	Subunit	Proof-of-concept ECaB	Subunit engineered ECaB
Operation time (h)	NO_3^- extraction	96 h	24 h
	TAN production	30 h	8 h
	TAN recovery	72 h	24 h
	Total	96 h	48 h
Rate ($\mu\text{g N cm}^{-2} \text{h}^{-1}$)	NO_3^- extraction	10.4 ± 0.1	151.6
	TAN production	15.7 ± 0.9	319.6
	TAN recovery	6.0 ± 0.2	45.8
Energy consumption (kW h kg N^{-1})	NO_3^- extraction	0 (39.0 \pm 0.2 considering all subunits)	0 (48.2 considering all subunits)
	TAN production	81.9 \pm 3.5	67.2
	TAN recovery	90.0 \pm 2.7	295.3
Efficiency (%)	NO_3^- extraction ($\eta_{\text{NO}_3^- \text{ extraction}}$)	98.1 \pm 0.3%	67.5%
	TAN production (Y_{TAN})	$49.0 \pm 2.6\%$	82.5%
	TAN recovery ($\eta_{\text{TAN recovery}}$)	$91.0 \pm 2.1\%$	22.8%

systems. ECaB's primary function (wastewater treatment) can be offset by its ability to recover chemical value, so we determined target j_{TAN} values that would allow Co(DIM) in the ECaB system to be a net-zero cost over a ten year lifetime treating wastewater NO_3^- from a large wastewater treatment plant ($1 \times 10^6 \text{ gal}_{\text{wastewater day}^{-1}}$)⁵⁹ (Fig. 7a, Section S7.2, ESI†). Our assessment is conservative because it considered revenue from $(\text{NH}_4)_2\text{SO}_4$ fertilizer but did not consider other financial

incentives of ECaB in a wastewater treatment process, such as water recovery revenue, conventional nitrogen treatment costs, or avoided regulatory fines for environmental NO_3^- discharge. The calculated difference between target j_{TAN} and our experimental j_{TAN} describes the gap in reactor-level catalytic activity required for ECaB process feasibility. Using the same FE_{TAN} , $\eta_{\text{NO}_3\text{RR}}$, and $\eta_{\text{anode, membrane}}$ observed in subunit engineered ECaB, the required j_{TAN} for the unit process to be a net-zero cost

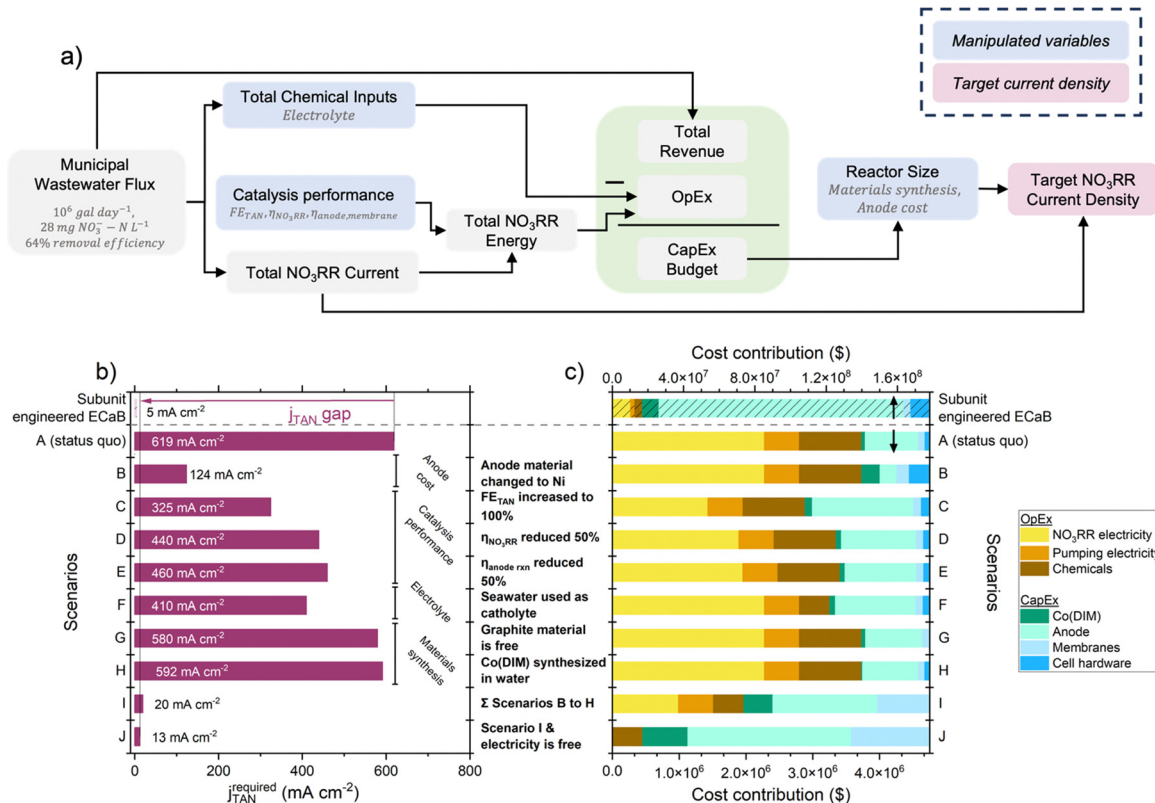


Fig. 7 (a) Flow diagram for simplified cost assessment of Co(DIM)-mediated NO₃RR in ECaB. The flux of wastewater NO₃⁻ from a large wastewater treatment plant (1 × 10⁶ gal_{wastewater} day⁻¹, 28 mg NO₃⁻-N L⁻¹ influent treated to 10 mg NO₃⁻-N L⁻¹ effluent = 64% removal efficiency to meet the EPA standard for drinking water)⁵⁹ was used as a basis for the operating expenditures (OpEx; chemical costs, NO₃RR electricity costs, and pumping electricity costs), capital expenditure (CapEx), and revenue of a scaled-up ECaB system. The difference between the net present values of revenue and expenditures was set to zero to determine the CapEx budget. The entire CapEx budget was spent on Co(DIM), anode material, membrane material, and cell hardware material, which defined the geometric surface area required. The total current was divided by the surface area to obtain j_{TAN} . Detailed calculations are provided in Section S7.2 (ESI†). (b) TAN current density (j_{TAN} ; red) for experimental ECaB performance (this work, Co(DIM)-ECaB) and for scenario-specific performance targets. In all scenarios, the cost of electricity was € 3 kW h⁻¹.⁶² For Co(DIM)-ECaB and scenario A, FE_{TAN} was 62.9% and E_{cell} was 2.7 V (η_{NO_3RR} was 0.905 V and $\eta_{anode,rxn}$ was 0.765, calculated from the pH-dependent equilibrium potentials of the NO₃RR and OER). With improvements to catalysis thermodynamic performance, electrolytes, and materials synthesis, the target current density for Co(DIM)-ECaB to be a net zero cost is decreased by 31.0 times (from 619 mA cm⁻² to 20.0 mA cm⁻²). If electricity becomes a free utility, this target can be further reduced to 13 mA cm⁻². (c) Cost contribution of OpEx (chemical inputs, NO₃RR electricity, and pumping electricity) and CapEx (Co(DIM), anodes, membranes, and cell hardware) to the overall system.

was 619 mA cm⁻² (120× that of our experimental value; Fig. 7b). While this gap is large, it can be overcome by engineering anode cost (scenario B), thermodynamic performance (scenarios C–E), electrolyte identity (scenario F), and materials synthesis (scenarios G and H). Anode cost played the largest role in reducing the target j_{TAN} due to the high cost of platinum-group metals; nickel-based anodes are under active investigation as lower-cost oxygen evolution anode materials.^{60,61} FE_{TAN} played the second largest role in reducing target j_{TAN} and could be addressed by unit process-level development (e.g., enhancing NO₃⁻ up-concentration to its thermodynamic limit). Seemingly innocuous changes had large contributions to reducing target j_{TAN} (e.g., using seawater as a catholyte reduced target j_{TAN} by 33.8%). In the limit where all scenarios B–H are achieved and electricity is a free utility (i.e., scenario J), the target j_{TAN} is 2.46× our subunit engineered ECaB j_{TAN} . The dominant cost contribution to j_{TAN} targets in scenarios A–H (Fig. 7c) was operational expenditures (OpEx, specifically electricity for

NO₃RR). Only in scenario I, when anode cost, FE_{TAN} , η_{NO_3RR} , and $\eta_{anode,membrane}$ were improved together, did capital expenditures (CapEx) outweigh OpEx. Meanwhile, Co(DIM) synthesis was a minority cost contributor in all scenarios, indicating that homogenous catalysts like Co(DIM) can be financially feasible and that efforts to reduce the overall system cost should prioritize engineering reaction potentials and FEs. Practically, our cost analysis highlights that overcoming limitations of reaction thermodynamics, electrolyte engineering, and materials synthesis can significantly reduce gaps between experimental and target j_{TAN} of scalable systems.

In addition to converting wastewater NO₃⁻ to purified TAN at unprecedented energy efficiency, ECaB also provides a generalizable, modular platform for benchmarking electrocatalysis. For example, we performed Co(DIM)-mediated nitrite reduction in ECaB with a simplified wastewater feed containing NO₂⁻, achieving a TAN yield of 71.0% in 2 hours of CPE (Fig. S39, ESI†). ECaB could similarly be used for CO₂ reduction

(homogeneous or heterogeneous) from $\text{HCO}_3^-/\text{CO}_3^{2-}$ feeds. The ECaB platform and our cost assessment could be adapted to other homogeneous and heterogeneous catalysts, electrodes, membranes, mass transport conditions, and operating parameters in specific wastewaters. Performing both extraction and recovery *via* membranes facilitates comparison of co-dependent reaction and separation rates and efficiencies (Tables S4–S7, ESI†).³³ Volume reduction of NO_3^- -containing electrolytes by low-energy separations processes like DD could help remediate the majority of NO_3^- emissions contributed by high volume, dilute NO_3^- sources. The combination of subunit processes in ECaB driven by only one electrochemical power source will integrate well with distributed renewable power generation and storage.⁶³ ECaB is therefore a promising and practical platform to investigate modular and on-site reactive separations.

3. Conclusions

In this study, we elucidated catalytically influential wastewater constituents (specifically Mg^{2+}) and their effects on a homogeneous NO_3RR catalyst's (Co(DIM)) performance to rationally design a novel reactive separations process: electrocatalyst-in-a-box (ECaB). Iteratively investigating reactor-scale performance and microenvironment-scale interfacial phenomena provided design principles for a system resilient to wastewater impurities, which we systematically investigated using simplified, simulated, and real wastewaters. The presence of Mg^{2+} in real NO_3^- -bearing secondary effluent inhibited NO_3RR activity but did not affect NO_3RR selectivity or FE. Mg deposition on the cathode surface was shown to be the major passivation mechanism, aligned with recent heterogeneous NO_3RR reports of water hardness passivating cathodes.¹⁶ Heterogeneous electron transfer between the cathode and homogeneous Co(DIM) was slowed by the passivated surface, but the homogeneous NO_3RR reaction was not observably affected. We showed that Co(DIM) can protect the cathode from inhibition by preventing specific adsorption of Mg^{2+} . We also showed that anion-selective separations *via* DD enable cathode protection along with homogeneous catalyst reuse and treated water recovery. Combining DD and NO_3RR within the ECaB process demonstrated promising wastewater NO_3^- extraction, NO_3^- conversion to TAN, and TAN recovery as a purified product. Proof-of-concept ECaB achieved $98.1 \pm 0.3\%$ NO_3^- -N removal from a real municipal secondary effluent and recovered a pure TAN product with the lowest reported energy consumption to date for an NO_3RR system ($90.0 \pm 2.7 \text{ kW h kg N}^{-1}$). Subunit engineered ECaB enabled a sustained j_{TAN} of $5.14 \text{ mA cm}_{\text{geometric}}^{-2}$ for 8 h of Co(DIM)-mediated NO_3RR with low energy consumption maintained ($67.2 \text{ kW h kg N}^{-1}$ for TAN production). A cost assessment showed that subunit engineered ECaB j_{TAN} must be improved by $120\times$ to meet *status quo* performance targets, but that tractable improvements to catalysts, electrolytes, and materials in ECaB systems can reduce targets to $2.46\times$ the j_{TAN} we achieved in subunit engineered ECaB.

This work encourages the use-informed study of molecular catalysts and integrated unit process analysis for wastewater refining. The development of ECaB was informed entirely by

the composition of a generalizable NO_3^- -rich wastewater, underscoring the imperative, insightful connections between systematic wastewater-based electrochemical research and the value propositions (*i.e.*, pollutant removal and product generation) posed by a novel unit process. The developed ECaB architecture can also serve as a platform for comparative investigations of wastewaters, catalysts, and reactor operating conditions. Deployment feasibility for NO_3RR reactive separations systems will be governed by analysis of efficiencies, rates, and energy consumption for extraction, conversion, and recovery unit processes.³ The study of integrated reactive separations that match the scale of wastewater- NO_3^- generation will accelerate use of wastewaters as feedstocks for electrified chemical production. Ultimately, this work innovates on incumbent centralized nitrogen management systems by producing commodities from impure, variable, and complex NO_3^- -rich wastewaters.

4. Methods

All chemicals were purchased as reagent grade and used as received. Nanopure water (resistivity: $18.2 \text{ M}\Omega \text{ cm}$) was used for all experiments and measurements unless stated otherwise. Before experiments, cation exchange membranes (CEM; CMI-7000, Membranes International Inc.) were stored in 0.1 M KClO_4 ; anion exchange membranes (AEM; ASVN, Selemion) were stored in nanopure water; and bipolar membranes (BPM; FBM, Fuma-sep) were stored in 1 M NaCl . Hydrophobic gas-permeable membranes (GPM; CLARCOR QP 952 (polytetrafluoroethylene), CLARCOR Industrial Air) were used as received.

4.1. Catalyst synthesis and characterization

The perchlorate salt of $[\text{Co}(\text{DIM})\text{Br}_2]^+$ (Fig. 8) was prepared as detailed previously.²⁹ ^1H NMR spectra (Varian Inova 600 at 600 MHz; Fig. S1, ESI†) and LC-MS spectra (Agilent 1260 HPLC with an Agilent 6460 Triple Quadrupole MS; Fig. S2, ESI†) of Co(DIM) confirmed the anticipated structure, molecular weight, and axial ligation of the catalyst.

4.2. Electrochemical methods

A BioLogic VMP-300 potentiostat was used to control the potential applied to the working electrode *versus* the reference electrode. All electrochemical experiments were recorded using 85% IR compensation based on the ohmic resistance obtained *via* potentiostatic electrochemical impedance spectroscopy.

4.2.1. Cyclic voltammetry (CV) and rotating-disk electrode (RDE) controlled-potential electrolysis (CPE). All CV and RDE CPE experiments were conducted in a 5-port glass RDE cell (Pine Research). The working electrode was a 5 mm glassy carbon (GC) disk (Pine Research), the counter electrode was a 6.4 mm diameter graphite rod in a glass tube with a Teflon frit (Pine Research), and the reference electrode was a Ag/AgCl electrode (Pine Research, 4.0 M KCl). The 5 mm GC electrode was polished with $1 \mu\text{m}$ alumina slurry (BASi) in a figure-eight motion on a microcloth polishing pad (BASi) for one minute. After polishing, the GC electrode was sonicated in nanopure

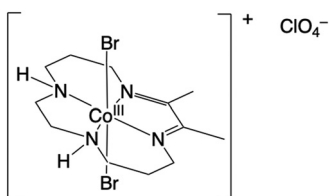


Fig. 8 The structure of Co(DIM) in its synthesized, crystalline form.

water for one minute and blow dried with N_2 . All CVs were collected at 100 mV s^{-1} and the first sweep of each CV is shown. All CVs began at the open circuit potential (OCP) and were swept to the first switching potential of $-1.2 \text{ V vs. Ag/AgCl}$, then swept to the second switching potential of $+0.6 \text{ V vs. Ag/AgCl}$, then swept back to OCP. RDE CPEs were performed using an electrode rotator (Pine Research). During dosing experiments, $28 \mu\text{L}$ of 1 M MgCl_2 , $30 \mu\text{L}$ of 1 M NaHCO_3 , or $38 \mu\text{L}$ of 1 M CaCl_2 were manually pipetted into 20 mL of electrolyte *via* a glass port in the cell. The injected volumes of 1 M salt solutions were such that each species (Mg^{2+} , Ca^{2+} , HCO_3^-) concentration in the 20 mL of electrolyte matched the concentration in the real wastewater.

4.2.2. Two-chamber controlled-potential electrolysis (CPE). Two-chamber CPE experiments were performed in a polycarbonate compression cell separated by a CEM and held together with stainless steel bolts. Each chamber had a volume of $\sim 7 \text{ mL}$ and a chamber cross-sectional area of 5.4 cm^2 . The working electrode (cathode) was a type II GC plate (ThermoFisher Scientific) and was stored in $1 \text{ M H}_2\text{SO}_4$ when not in use to remove any trace metal impurities. Before CPE, the GC electrode was prepared in the same manner as described in Section 4.2.1. The counter electrode (anode) was a mixed metal oxide (MMO) iridium-tantalum mesh (Titan Metal Fabricators). The geometric cross-sectional area of the cathode, anode, and CEM were 5.4 cm^2 . The reference electrode was a leakless Ag/AgCl electrode (3.4 M KCl ; ET072, eDAQ) calibrated against a master reference electrode (4.0 M KCl ; Fisherbrand accumet) and was inserted into the cathode chamber *via* a threaded port. Three catholytes were tested: simplified wastewater, simulated wastewater, and real wastewater (Table S1, ESI†). The anolyte was 0.1 M KClO_4 in all experiments. 50 mL of each electrolyte were recirculated in batch at a volumetric flow rate of 3.5 mL min^{-1} (linear flow rate in each chamber: 1.75 cm min^{-1}) to match our previous investigation of Co(DIM).³⁸ Buffers were not used in CPE because previous investigations showed that Co(DIM)-mediated NO_3RR catalysis is inhibited by common inorganic (phosphate, carbonate/bicarbonate) buffers;²⁸ we also tried common “non-coordinating” buffers (TRIS, MOPS, borax) but observed no catalysis in CV or CPE.

The statistical significance of differences between the observed CPE performance in the three catholytes was compared using paired *t*-tests for equal means, where we rejected the null hypothesis (difference between CPE performance results from a normal distribution with mean equal to zero and unknown variance) if $p < 0.05$.

Rinse tests were performed to assess the catalytic activity of deposits on GC cathodes. The cell was then reconstructed with the deposit-containing GC electrode. An eight-hour CPE was

performed (identical operation to the first CPE) with 50 mL simplified wastewater without dissolved Co(DIM) in the catholyte (*i.e.*, 0 mM Co(DIM) , 6.2 mM NaCl , 2 mM NaNO_3).

4.2.3. Proof-of-concept electrocatalyst-in-a-box (ECaB). The ECaB reactor consisted of two compression cells: a two-chamber cell for electrocatalysis and a three-chamber cell for Donnan dialysis and ammonia gas stripping (Fig. S3, ESI†). The compression cell pieces were the same as used in two-chamber CPE experiments. Four electrolyte reservoirs (200 mL wastewater, 50 mL catholyte, 50 mL trap solution, and 50 mL anolyte) were recirculated in batch mode through the two cells. The only solution to recirculating between both cells was using the catholyte to facilitate the three subunit processes of NO_3^- -extraction by Donnan dialysis, NO_3^- -conversion to TAN by Co(DIM)-mediated NO_3RR , and TAN recovery by membrane stripping. In the Donnan dialysis and ammonia gas stripping cell, the wastewater and catholyte were separated by an AEM (to facilitate NO_3^- extraction) and the catholyte and trap solution were separated by a GPM (to facilitate TAN recovery). The electrocatalysis cell contained a GC plate cathode (to facilitate NO_3^- conversion to TAN), a MMO iridium-tantalum mesh anode (the same as described in 4.2.2), and a leakless reference electrode; the catholyte and anolyte were separated by a BPM. The flow rate was 3.5 mL min^{-1} for the electrocatalysis cell, and the flow rate was 28 mL min^{-1} for the Donnan dialysis and ammonia gas stripping cell. During ECaB operation, the electrocatalytic cell was alternated between open circuit ($0\text{--}24 \text{ h}$, $34\text{--}48 \text{ h}$, $58\text{--}72 \text{ h}$, $82\text{--}96 \text{ h}$) and $-1.05 \text{ V}_{\text{Ag/AgCl}}$ ($24\text{--}34 \text{ h}$, $48\text{--}58 \text{ h}$, $72\text{--}82 \text{ h}$).

4.2.4. Subunit engineered ECaB. In a second iteration of ECaB experiments, a commercial serpentine flow field electrolyzer (Fuel Cell Technologies, 10 cm^2) was used for both Donnan dialysis and electrocatalysis. Donnan dialysis was performed first in the electrolyzer; then the electrolyzer was disassembled and reassembled to perform electrocatalysis. In Donnan dialysis, an AEM was sandwiched between the two graphite flow field blocks. 2 L of municipal secondary effluent was used as the wastewater feed and 50 mL of 1 M KCl with 8 mM Co(DIM) was used as the receiving solution. The flow rate was 57 mL min^{-1} . In electrocatalysis, a CEM was sandwiched between the graphite flow field blocks and a pseudo reference electrode (a $250 \mu\text{m}$ Ag wire anodized in saturated KCl) was attached to the CEM. The graphite flow block was used as the cathode. The anode was a platinized Ti mesh (Fuel Cell Store) in electrical contact with the anode graphite flow block. The catholyte was the resulting solution from Donnan dialysis and the anolyte was 50 mL of 0.1 M KClO_4 . The flow rate was 3.5 mL min^{-1} in the electrolyzer. -1.05 V *vs. Ag/AgCl* was applied in 1 hour increments. After each increment, the catholyte was adjusted back to pH 6 with $\sim 200 \mu\text{L}$ 10 wt\% HCl to keep Co(DIM) in its stable operating pH regime.^{28,38} A separate two-chamber 5.4 cm^2 compression cell was assembled to house the GPM for TAN recovery with 50 mL of $0.1 \text{ M H}_2\text{SO}_4$ as the trap solution; TAN recovery was run in parallel with electrocatalysis at a flow rate of 28 mL min^{-1} .

4.3. Aqueous characterization

Aqueous ion speciation was quantified with cation chromatography (Na^+ , NH_4^+ , K^+ , Ca^{2+} , Mg^{2+}) and anion chromatography

(Cl^- , NO_2^- , NO_3^- , SO_4^{2-} , PO_4^{3-}). Both cation chromatography (4 mM tartaric acid/2 mM oxalic acid eluent, SCS 1 column at 30 °C) and anion chromatography (4.5 mM carbonate/0.8 mM bicarbonate eluent, AS23-4 μm column at 30 °C) were performed with a dual Dionex ICS-6000 system (ThermoFisher Scientific). For ECaB, the high concentration of K^+ in the catholyte made quantification of TAN by cation chromatography difficult, so flow injection analysis (indophenol method) was conducted with a SEAL AA500 AutoAnalyzer.³⁸ For both cation chromatography and flow injection analysis, aliquots above pH 7 were acidified to prevent ammonia volatilization and facilitate accurate quantification of the measure of total ammonia nitrogen (TAN: sum of aqueous ammonium, NH_4^+ , and aqueous ammonia, NH_3). Inductively coupled plasma mass spectrometry (ICP-MS) was used to quantify the concentration of ⁵⁹Co in each ECaB chamber at the initial and final time points. ICP-MS (ThermoFisher Scientific) was performed using a parallel flow nebulizer (Burgener PEEK Mira Mist) and a Peltier-cooled Scott-type double pass cyclonic spray chamber cooled to 2.7 °C.⁶⁴

4.4. Electrode characterization

X-ray photoelectron spectroscopy (XPS) was performed using a Phi Versaprobe 3 with monochromatized Al $\text{K}\alpha$ (1486 eV) radiation. Scanning electron microscopy (SEM) and energy dispersive X-ray spectroscopy (EDS) characterization was performed on a Thermo Fisher Scientific Apreo S LoVac (5 kV, 5.0 pA) with a Bruker Quantax EBSD 400i integrated system containing an XFlash 6|60 SDD EDS detector. Raw EDS data were processed and plotted with Bruker's ESPRIT software.

4.5. Efficiency, rate, and energy comparison with the literature

The scope of our comparison to precedent literature was constrained to literature studies that investigated reactive separations in real wastewaters. Reported values of efficiencies, rates, and energy consumption are shown for the four subunit processes of nitrate extraction (Table S4, ESI†), nitrate conversion by the NO_3RR (Table S5, ESI†), TAN production by the NO_3RR (Table S6, ESI†), and TAN recovery (Table S7, ESI†). Efficiencies, rates, and energy consumption were shown by Kogler and co-workers to be the most important operational metrics for wastewater treatment practitioners to make technology decisions for future systems.⁴⁹

Data availability

Data for this article are available at Stanford Digital Repository at <https://doi.org/10.25740/sk954gp2933>. These data include NMR and XPS spectra, aqueous nitrate and ammonia/ammonium mass balances for controlled-potential electrolysis and electrocatalyst-in-a-box (ECaB) experiments, electrochemical data used to calculate energy consumption for ECaB experiments, and worksheet and tabulated results of ECaB cost assessment.

Conflicts of interest

There are no conflicts to declare.

Acknowledgements

We are grateful to several funders of this work, including the National Science Foundation EFRI program (Award 2132007), the Dreyfus Foundation (Camille Dreyfus Teacher-Scholar Award), the Sustainability Accelerator within the Doerr School of Sustainability at Stanford University, and the Chemical Engineering Department at Stanford University. D. M. M. acknowledges support from the National Aeronautics and Space Administration (NASA) Space Technology Graduate Research Opportunities fellowship (Award 80NSSC22K1191). M. J. L. acknowledges support from the Northern California Chapter of the Achievement Rewards for College Scientists (ARCS) Foundation. K. A. acknowledges support from the Stanford Graduate Fellowship. A.K. acknowledges support from the Stanford Interdisciplinary Graduate Fellowship. Part of this work was performed at the Stanford Nano Shared Facilities (SNSF), supported by the National Science Foundation under award ECCS-2026822. The authors thank Gaurav Kamat for the ICP-MS analysis, Jinyu Guo for the XRD analysis and for her thoughtful engagement with this work, and the Tarpeh Laboratory for their support, feedback, and inspiration.

References

- 1 C. Smith, A. K. Hill and L. Torrente-Murciano, *Energy Environ. Sci.*, 2020, **13**, 331–344.
- 2 J. Lim, C. A. Fernández, S. W. Lee and M. C. Hatzell, *ACS Energy Lett.*, 2021, **6**, 3676–3685.
- 3 D. M. Miller, K. Abels, J. Guo, K. S. Williams, M. J. Liu and W. A. Tarpeh, *J. Am. Chem. Soc.*, 2023, **145**, 19422–19439.
- 4 J. Zhou, P. R. Leavitt, Y. Zhang and B. Qin, *Water Res.*, 2022, **221**, 118728.
- 5 J. Merder, T. Harris, G. Zhao, D. M. Stasinopoulos, R. A. Rigby and A. M. Michalak, *Nat. Water*, 2023, **1**, 844–854.
- 6 W. K. Dodds, W. W. Bouska, J. L. Eitzmann, T. J. Pilger, K. L. Pitts, A. J. Riley, J. T. Schloesser and D. J. Thornbrugh, *Environ. Sci. Technol.*, 2009, **43**, 12–19.
- 7 The Challenge of Tracking Nutrient Pollution 2300 Miles|U.S. Geological Survey, <https://www.usgs.gov/news/challenge-tracking-nutrient-pollution-2300-miles>, (accessed February 4, 2022).
- 8 M. Lang, P. Li and X. Yan, *Sci. Total Environ.*, 2013, **458–460**, 238–245.
- 9 T. Kato, H. Kuroda and H. Nakasone, *J. Hydrol.*, 2009, **368**, 79–87.
- 10 B. Eghball and J. E. Gilley, *J. Environ. Qual.*, 1999, **28**, 1201–1210.
- 11 C. D. A. McLay, R. Dragten, G. Sparling and N. Selvarajah, *Environ. Pollut.*, 2001, **115**, 191–204.
- 12 R. K. Hubbard and J. M. Sheridan, *J. Environ. Qual.*, 1983, **12**, 291–295.
- 13 Z.-H. Wang and S.-X. Li, in *Advances in Agronomy*, ed. D. L. Sparks, Academic Press, 2019, vol. 156, pp. 159–217.

14 J. M. McEnaney, S. J. Blair, A. C. Nielander, J. A. Schwalbe, D. M. Koshy, M. Cargnello and T. F. Jaramillo, *ACS Sustainable Chem. Eng.*, 2020, **8**, 2672–2681.

15 S.-E. Bae, K. L. Stewart and A. A. Gewirth, *J. Am. Chem. Soc.*, 2007, **129**, 10171–10180.

16 A. Atrashkevich, A. S. Fajardo, P. Westerhoff, W. S. Walker, C. M. Sánchez-Sánchez and S. Garcia-Segura, *Water Res.*, 2022, **225**, 119118.

17 F.-Y. Chen, Z.-Y. Wu, S. Gupta, D. J. Rivera, S. V. Lambeets, S. Pecaut, J. Y. T. Kim, P. Zhu, Y. Z. Finfrock, D. M. Meira, G. King, G. Gao, W. Xu, D. A. Cullen, H. Zhou, Y. Han, D. E. Perea, C. L. Muhich and H. Wang, *Nat. Nanotechnol.*, 2022, **17**, 759–767.

18 J. Li, G. Zhan, J. Yang, F. Quan, C. Mao, Y. Liu, B. Wang, F. Lei, L. Li, A. W. M. Chan, L. Xu, Y. Shi, Y. Du, W. Hao, P. K. Wong, J. Wang, S.-X. Dou, L. Zhang and J. C. Yu, *J. Am. Chem. Soc.*, 2020, **142**, 7036–7046.

19 J. Lim, C.-Y. Liu, J. Park, Y.-H. Liu, T. P. Senftle, S. W. Lee and M. C. Hatzell, *ACS Catal.*, 2021, **11**, 7568–7577.

20 P. Li, Z. Jin, Z. Fang and G. Yu, *Energy Environ. Sci.*, 2021, **14**, 3522–3531.

21 Z.-Y. Wu, M. Karamad, X. Yong, Q. Huang, D. A. Cullen, P. Zhu, C. Xia, Q. Xiao, M. Shakouri, F.-Y. Chen, J. Y. (Timothy) Kim, Y. Xia, K. Heck, Y. Hu, M. S. Wong, Q. Li, I. Gates, S. Siahrostami and H. Wang, *Nat. Commun.*, 2021, **12**, 2870.

22 J. Li, M. Li, N. An, S. Zhang, Q. Song, Y. Yang and X. Liu, *Proc. Natl. Acad. Sci.*, 2021, **118**, e2105628118.

23 R. Jia, Y. Wang, C. Wang, Y. Ling, Y. Yu and B. Zhang, *ACS Catal.*, 2020, **10**, 3533–3540.

24 Y. Wang, W. Zhou, R. Jia, Y. Yu and B. Zhang, *Angew. Chem., Int. Ed.*, 2020, **59**, 5350–5354.

25 Y. Wang, A. Xu, Z. Wang, L. Huang, J. Li, F. Li, J. Wicks, M. Luo, D.-H. Nam, C.-S. Tan, Y. Ding, J. Wu, Y. Lum, C.-T. Dinh, D. Sinton, G. Zheng and E. H. Sargent, *J. Am. Chem. Soc.*, 2020, **142**, 5702–5708.

26 G.-F. Chen, Y. Yuan, H. Jiang, S.-Y. Ren, L.-X. Ding, L. Ma, T. Wu, J. Lu and H. Wang, *Nat. Energy*, 2020, **5**, 605–613.

27 J. G. Chen, R. M. Crooks, L. C. Seefeldt, K. L. Bren, R. M. Bullock, M. Y. Daresbourg, P. L. Holland, B. Hoffman, M. J. Janik, A. K. Jones, M. G. Kanatzidis, P. King, K. M. Lancaster, S. V. Lymar, P. Pfromm, W. F. Schneider and R. R. Schrock, *Science*, 2018, **360**, eaar6611.

28 S. Xu, D. C. Ashley, H.-Y. Kwon, G. R. Ware, C.-H. Chen, Y. Losovyy, X. Gao, E. Jakubikova and J. M. Smith, *Chem. Sci.*, 2018, **9**, 4950–4958.

29 S. C. Jackels, Keith Farmery, E. Kent Barefield, N. J. Rose and D. H. Busch, *Inorg. Chem.*, 1972, **11**, 2893–2901.

30 D. J. Cole-Hamilton, *Science*, 2003, **299**, 1702–1706.

31 K. Hu, P. Zhou, Y. Yang, T. Hall, G. Nie, Y. Yao, X. Duan and S. Wang, *ACS ES&T Eng.*, 2022, **2**, 110–120.

32 J. Sun, S. Jennekelli, M. Lee, A. Jones, D. M. O'Carroll, M. J. Manefield, M. Bhadbhade, B. Åkermark, B. Das and N. Kumar, *Environ. Sci. Technol.*, 2022, **56**, 7830–7839.

33 V. A. Niemann, P. Benedek, J. Guo, Y. Xu, S. J. Blair, E. R. Corson, A. C. Nielander, T. F. Jaramillo and W. A. Tarpeh, *ACS Catal.*, 2023, **13**, 6268–6279.

34 J. Gao, N. Shi, Y. Li, B. Jiang, T. Marhaba and W. Zhang, *Environ. Sci. Technol.*, 2022, **56**, 11602–11613.

35 J. Gao, N. Shi, X. Guo, Y. Li, X. Bi, Y. Qi, J. Guan and B. Jiang, *Environ. Sci. Technol.*, 2021, **55**, 10684–10694.

36 W. Zheng, L. Zhu, Z. Yan, Z. Lin, Z. Lei, Y. Zhang, H. Xu, Z. Dang, C. Wei and C. Feng, *Environ. Sci. Technol.*, 2021, **55**, 13231–13243.

37 K. Kim, A. Zagalskaya, J. L. Ng, J. Hong, V. Alexandrov, T. A. Pham and X. Su, *Nat. Commun.*, 2023, **14**, 823.

38 M. J. Liu, D. M. Miller and W. A. Tarpeh, *Environ. Sci. Technol. Lett.*, 2023, **10**, 458–463.

39 J. M. Savéant and C. Costentin, *Elements of molecular and biomolecular electrochemistry: an electrochemical approach to electron transfer chemistry*, Wiley, Hoboken, NJ, Second edn, 2019.

40 J. Guo, P. Brimley, M. J. Liu, E. R. Corson, C. Muñoz, W. A. Smith and W. A. Tarpeh, *ACS Sustainable Chem. Eng.*, 2023, **11**, 7882–7893.

41 I. Bhugun, D. Lexa and J.-M. Savéant, *J. Phys. Chem.*, 1996, **100**, 19981–19985.

42 A. Pérez-González, A. M. Urtiaga, R. Ibáñez and I. Ortiz, *Water Res.*, 2012, **46**, 267–283.

43 R. Mohammadi, D. L. Ramasamy and M. Sillanpää, *Desalination*, 2021, **498**, 114726.

44 S. A. Hawks, M. R. Cerón, D. I. Oyarzun, T. A. Pham, C. Zhan, C. K. Loeb, D. Mew, A. Deinhart, B. C. Wood, J. G. Santiago, M. Stadermann and P. G. Campbell, *Environ. Sci. Technol.*, 2019, **53**, 10863–10870.

45 H. Chen, M. Rose, M. Fleming, S. Souizi, U. Shashvatt and L. Blaney, *Chem. Eng. J.*, 2023, **455**, 140522.

46 M. J. Pennino, S. G. Leibowitz, J. E. Compton, R. A. Hill and R. D. Sabo, *Sci. Total Environ.*, 2020, **722**, 137661.

47 D. B. Shah and G. A. Coulman, *Biotechnol. Bioeng.*, 1978, **20**, 43–72.

48 M. Janssen, C. Müller and D. Vogt, *Green Chem.*, 2011, **13**, 2247–2257.

49 A. Kogler, M. Farmer, J. A. Simon, S. Tilmans, G. F. Wells and W. A. Tarpeh, *ACS ES&T Eng.*, 2021, **1**, 662–684.

50 G. Soloveichik, *Nat. Catal.*, 2019, **2**, 377–380.

51 D. Wu, X. Li and X. Li, *ACS ES&T Water*, 2021, **1**, 796–807.

52 US Department of Agriculture, Pacific Northwest Production Cost Report (Bi-Weekly), <https://usda.library.cornell.edu/concern/publications/h989sc11z?locale=en>, (accessed June 5, 2024).

53 P. Gayen, J. Spataro, S. Avasarala, A.-M. Ali, J. M. Cerrato and B. P. Chaplin, *Environ. Sci. Technol.*, 2018, **52**, 9370–9379.

54 J. Wang, S. Wang, Z. Zhang and C. Wang, *J. Environ. Manage.*, 2020, **276**, 111357.

55 H. Cheng, K. Scott and P. A. Christensen, *Chem. Eng. J.*, 2005, **108**, 257–268.

56 I. Katsounaros, M. Dortsiou and G. Kyriacou, *J. Hazard. Mater.*, 2009, **171**, 323–327.

57 N. Lazouski, A. Limaye, A. Bose, M. L. Gala, K. Manthiram and D. S. Mallapragada, *ACS Energy Lett.*, 2022, **7**, 2627–2633.

58 C. A. Fernandez and M. C. Hatzell, *J. Electrochem. Soc.*, 2020, **167**, 143504.

59 K. E. Kapo, M. Paschka, R. Vamshi, M. Sebasky and K. McDonough, *Sci. Total Environ.*, 2017, **603–604**, 445–452.

60 E. K. Volk, S. Kwon and S. M. Alia, *J. Electrochem. Soc.*, 2023, **170**, 064506.

61 Z.-Y. Wu, F.-Y. Chen, B. Li, S.-W. Yu, Y. Z. Finfrock, D. M. Meira, Q.-Q. Yan, P. Zhu, M.-X. Chen, T.-W. Song, Z. Yin, H.-W. Liang, S. Zhang, G. Wang and H. Wang, *Nat. Mater.*, 2023, **22**, 100–108.

62 W. J. Cole, B. A. Frew, P. J. Gagnon, J. Richards, Y. Sun, R. M. Margolis and M. A. Woodhouse, *SunShot 2030 for Photovoltaics (PV): Envisioning a Low-cost PV Future*, 2017.

63 C. A. Fernández, O. Chapman, M. A. Brown, C. E. Alvarez-Pugliese and M. C. Hatzell, *Environ. Sci. Technol.*, 2024, **58**, 6964–6977.

64 D. H. Marin, J. T. Perryman, M. A. Hubert, G. A. Lindquist, L. Chen, A. M. Aleman, G. A. Kamat, V. A. Niemann, M. B. Stevens, Y. N. Regmi, S. W. Boettcher, A. C. Nielander and T. F. Jaramillo, *Joule*, 2023, **7**, 765–781.